J|A|C|S COMMUNICATIONS

Published on Web 01/07/2010

Resistance Switching in Electrodeposited Magnetite Superlattices

Jay A. Switzer,* Rakesh V. Gudavarthy, Elizabeth A. Kulp, Guojun Mu, Zhen He, and Andrew J. Wessel

Department of Chemistry and Graduate Center for Materials Research, Missouri University of Science and Technology, Rolla, Missouri 65409-1170

Received November 2, 2009; E-mail: jswitzer@mst.edu

As the size of nonvolatile memory continues to shrink, there is increasing demand for highly scalable memory devices. An emerging technology is resistive random access memory (RRAM) that is based on resistance switching in materials such as transition metal oxides.[1] Natelson and co-workers have shown that nanophase magnetite, Fe_3O_4, exhibits resistance switching,[2] which they attribute to an electric field driven insulator-to-metal phase transition below the Verwey temperature[3] of 120 K due to strong electron−phonon coupling. For such RRAM devices, it is often necessary to have nanophase material. Superlattices (that is, periodic layered nanostructures with coherent stacking of atomic planes) are ideal for such applications, because they combine the nanometer-scale dimensions of the individual layer thicknesses with the utility of large-scale films that can be conveniently connected to the real world. We previously demonstrated that it is possible to electrodeposit both defect chemistry and compositional ceramic superlattices.[4] Here, we show that defect chemistry superlattices based on Fe_3O_4 and compositional superlattices in the $Fe_3O_4/ZnFe_2O_4$ system can be electrodeposited as epitaxial films on Au(111) from a single plating bath by simply pulsing the applied potential. We designate superlattices based on Fe_3O_4 which have alternating layers with different Fe(III)/Fe(II) ratios as *defect chemistry* superlattices and superlattices in the $Fe_3O_4/ZnFe_2O_4$ system which have alternating layers with different Fe/Zn ratios as *compositional* superlattices. Due to the nanometer-scale thickness of the layers in the magnetite defect-chemistry superlattices, they exhibit a unique and potentially important multistate resistance switching during perpendicular transport measurements.

In the deposition of superlattices we exploit the fact that magnetite (Fe_3O_4) and zinc ferrite ($ZnFe_2O_4$) deposit by an electrochemical/chemical (EC) mechanism and that the surface concentrations of Fe(II) and Fe(III) can be precisely controlled through the applied potential. Films of Fe_3O_4 can be deposited with stoichiometries that depend on the applied potential. We deposit defect chemistry superlattices based on Fe_3O_4 from a stirred solution of 87 mM Fe(III), 100 mM triethanolamine (TEA), and 2 M NaOH at 80 °C. The deposition of Fe_3O_4 is believed to occur by an electrochemical−chemical (EC) mechanism described by eqs 1 and 2.[5]

$$Fe(TEA)^{3+} + e^- \rightarrow Fe^{2+} + TEA \quad (1)$$

$$Fe^{2+} + 2Fe(TEA)^{3+} + 8OH^- \rightarrow Fe_3O_4 + 2TEA + 4H_2O \quad (2)$$

A linear sweep voltammogram at 50 mV/s of a Au(111) single crystal in the stirred (200 rpm) deposition bath is shown in Figure 1A. The deposition of Fe_3O_4 begins at a potential of −0.99 V, and the reaction becomes mass-transport-limited at a potential of approximately −1.2 V vs Ag/AgCl. The mass-transport-limited

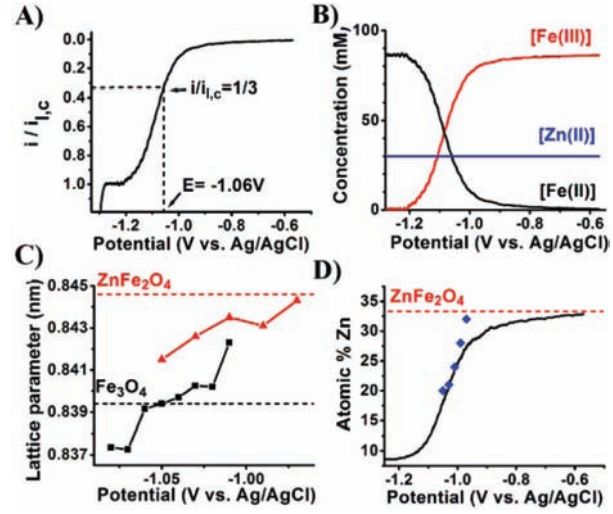

Figure 1. Using the applied potential to control the composition of magnetite and zinc ferrite films. (A) Linear sweep voltammogram in the Fe(III)-TEA bath used to produce magnetite defect chemistry superlattices. (B) Plot of the concentrations of Fe(III), Fe(II), and Zn(II) at the electrode surface as a function of potential for the alkaline Fe(III)-TEA bath with 30 mM Zn(II) added, which is used to produce compositional superlattices in the $Fe_3O_4/ZnFe_2O_4$ system. (C) Plot of the lattice parameters of magnetite (black squares) and films in the magnetite/zinc ferrite system (red triangles) as a function of applied potential. The literature values for the lattice parameters of stoichiometric Fe_3O_4 and $ZnFe_2O_4$ are shown as black and red horizontal dashed lines. (D) Comparison of the measured Zn concentration (blue diamonds) to the calculated Zn concentration (smooth black curve) for films in the $Fe_3O_4/ZnFe_2O_4$ system as a function of applied potential. The composition of stoichiometric $ZnFe_2O_4$ is shown as a horizontal dashed red line.

current is predominately controlled by convection. At low overpotentials where $i = 0$, the surface concentration of $Fe(TEA)^{3+}$ should be equal to the bulk concentration, whereas, at high overpotentials at which the current reaches the mass-transport limit, the surface concentration of $Fe(TEA)^{3+}$ should approach zero. The surface concentration of Fe(III) can be calculated from eq 3,

$$\frac{i}{i_{1,c}} = \frac{[C_{Fe(III)}(bulk) - C_{Fe(III)}(surface)]}{C_{Fe(III)}(bulk)} \quad (3)$$

where i is the measured current, $i_{l,c}$ is the limiting cathodic current, $C_{Fe(III)}(bulk)$ is the bulk concentration of Fe(III) in solution, and $C_{Fe(III)}(surface)$ is the Fe(III) concentration at the electrode surface.[6] Stoichiometric Fe_3O_4 should deposit at an applied potential of −1.06 V vs Ag/AgCl at which $i/i_{l,c} = 1/3$. The material should have an excess of Fe(III) at potentials more positive than −1.06 V and an excess of Fe(II) at potentials more negative than −1.06 V vs Ag/AgCl.

10.1021/ja909295y

Compositional superlattices in the $Fe_3O_4/ZnFe_2O_4$ system can be produced by adding 30 mM Zn(II) to the deposition bath. The Zn(II) is electrochemically inert (see Figure S1) in the potential range of deposition and will substitute for Fe(II) in the crystal structure. The Zn(II) concentration in the film should decrease as the current approaches the mass-transport limit, because the surface concentration of Fe(II) increases as the current is increased. The calculated surface concentrations of Fe(III), Fe(II), and Zn(II) are shown in Figure 1B. The dependence of the lattice parameters of Fe_3O_4 and $Zn_xFe_{3-x}O_4$ films on the applied potential is shown in Figure 1C. In reasonable agreement with our calculations, Fe_3O_4 deposited at approximately −1.05 to −1.06 V vs Ag/AgCl has a lattice parameter that agrees well with the literature value of Fe_3O_4. We also measured the Verwey transition of films grown at a series of potentials by transport measurements. The Verwey transition temperature reaches a maximum value of 123 K for a magnetite film deposited at −1.065 V vs Ag/AgCl, compared with 103 K for a film grown at −1.01 V vs Ag/AgCl. Because nonstoichiometry is known to lower the Verwey transition temperature, our results suggest that nearly stoichiometric magnetite is produced at a potential of −1.065 V vs Ag/AgCl. Films grown in the presence of Zn(II) have lattice parameters that approach the literature value of $ZnFe_2O_4$ at more positive potentials. The calculated and measured (by EDS) Zn content of the films as a function of potential are shown in Figure 1D. The Zn concentration was calculated by assuming that the Zn(II)/Fe(II) ratio in the film is the same as the ratio of the surface concentrations calculated in Figure 1B from the linear sweep voltammogram. The Zn content in the films decreases as the current approaches the mass-transport limit.

Defect chemistry superlattices based on Fe_3O_4 were deposited by pulsing the potential in the Fe(III)-TEA bath between −1.01 and −1.065 V vs Ag/AgCl. Compositional superlattices in the $Fe_3O_4/ZnFe_2O_4$ system were deposited from the same bath with 30 mM Zn(II) added by pulsing between −0.99 and −1.05 V vs Ag/AgCl. The superlattices were deposited as epitaxial films on single-crystal Au(111) substrates.

The layered structure of a compositional superlattice in the $Fe_3O_4/ZnFe_2O_4$ system is readily apparent in the high angle annular dark field (HAADF) image in Figure 2A that we obtained in a focused ion beam (FIB) microscope. The superlattice was designed to have a large modulation wavelength of 70 nm so that it could be easily imaged in the FIB. The light layers that are 25 nm thick correspond to the higher zinc content layer that was grown at −0.99 V vs Ag/AgCl. The darker layers that are 45 nm thick correspond to the lower zinc content material that was grown at −1.05 V vs Ag/AgCl.

The superlattices were also characterized by X-ray diffraction. Figure 2B shows the (311) X-ray pole figures of a compositional superlattice in the $Fe_3O_4/ZnFe_2O_4$ system with a modulation wavelength of 12.5 nm (left) and the Au(111) substrate (right). The superlattice was deposited from the Zn(II)-containing bath by pulsing between −0.99 V vs Ag/AgCl for 2.5 s and −1.05 V vs Ag/AgCl for 0.5 s. The X-ray pole figures show that the superlattice grows epitaxially on the Au(111). Both pole figures have sharp peaks at tilt angles of 29.5°, 58.5°, and 80°, but the peaks for the superlattice are rotated azimuthally by 180° relative to the Au(111) peaks. That is, the films grow with the same (111) out-of-plane orientation as the substrate, but they are rotated antiparallel in-plane. The epitaxial relationship of the films to the Au(111) substrate is $Fe_3O_4(111)[01\bar{1}]//Au(111)[0\bar{1}1]$.

X-ray diffraction provides direct evidence that these multilayered films are superlattices (that is, crystallographically coherent multilayers). Figure 2C and 2D show X-ray diffraction patterns of Fe_3O_4 superlattices with modulation wavelengths of 12.2, 20.6, and 25.8 nm and compositional superlattices in the $Fe_3O_4/ZnFe_2O_4$ system with modulation wavelengths of 12.5, 16.8, and 29.2 nm, respectively. The superperiodicity of the superlattices manifests itself as satellites around the (444) Bragg peak. The modulation wavelength, Λ, of the superlattices was calculated from the position of the satellites using eq 4, where λ is the wavelength of the X-ray source (Cu Kα = 0.15401 nm), L is the order of the satellite, and θ is the diffraction angle of satellite L.[4b] The satellites are more intense in the Zn-containing superlattices, due to the larger Z-contrast in those superlattices.

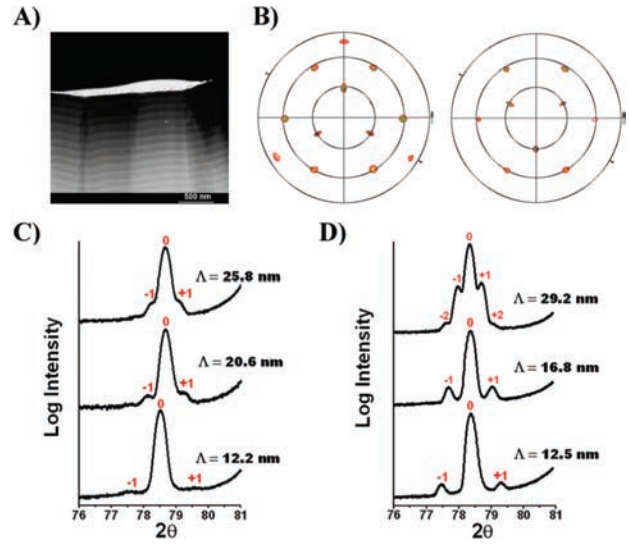

Figure 2. Electron microscopy and X-ray diffraction of electrodeposited superlattices. (A) STEM-high angle annular dark field image of zinc ferrite superlattice with a modulation wavelength of 70 nm. (B) (311) pole figures of zinc ferrite superlattice with 12.5 nm modulation wavelength (left) and Au(111) substrate (right). (C) 2θ scan around the (444) reflection for magnetite superlattices. (D) 2θ scan around the (444) reflection for zinc ferrite superlattices.

$$\Lambda = \frac{\lambda(L_1 - L_2)}{2(\sin\theta_1 - \sin\theta_2)} \qquad (4)$$

The electrodeposited defect-chemistry superlattices based on magnetite exhibit resistance switching during perpendicular transport measurements at 77 K. Resistance switching in bulk magnetite has been known since 1969.[7] Basically, a sample is maintained at a temperature (for example, 77 K) below the Verwey transition (120 K), at which the material is insulating. During a sweep of either the applied current or voltage, the magnetite undergoes an insulator-to-metal phase transition and the resistance sharply decreases. The high-to-low resistance switching in single-crystal magnetite has been attributed either to an insulator-to-metal transition driven by Joule heating due to the current flowing through the sample[7] or to an electric-field-driven transition due to the strong electron−phonon coupling.[2] Lee et al. presented strong evidence that the insulator-to-metal transition in nanophase magnetite is driven by the applied electric field.[2a]

For our resistance switching studies, a contact is made to the top of the superlattice and to the Au(111) single crystal using pressed In contacts (see inset of Figure 3). This configuration ensures perpendicular transport of charge through the sample. The sample is held below the Verwey transition by immersing it in liquid nitrogen at 77 K, and the bias is measured as the applied current is swept from 0 to 2 A at 50 mA/s. Figure 3 shows iV curves for two magnetite films grown at −1.01 and −1.065 V vs Ag/AgCl and a

superlattice produced by pulsing between −1.01 V for 1.5 s and −1.065 V vs Ag/AgCl for 0.5 s. The modulation wavelength of the superlattice is 12.2 nm (measured by X-ray diffraction), and it consists of 354 bilayers. The *iV* curve of the Fe(III)-rich film deposited at −1.01 V is nonohmic, but it shows no evidence of resistance switching. The *iV* curve of the Fe_3O_4 film deposited at −1.065 V has a similar nonohmic shape, except that it shows abrupt low-to-high resistance switching at applied biases of +0.95 and −0.93 V. This low-to-high resistance switching is not due to the insulating-to-metal phase transition that occurs at the Verwey transition. A similar transition has been observed in nanophase magnetite at room temperature.[8] Odagawa et al. attributed this low-to-high resistance switch to a field-driven oxidation of Fe_3O_4 to the less conductive γ-Fe_2O_3 (maghemite) at the interface between the metallic anode electrode and the Fe_3O_4.[8a] They detected maghemite at the interface using Raman spectroscopy. We assume that the low-to-high resistance switch that we observe in the Fe_3O_4 deposited at −1.065 V vs Ag/AgCl is also due to the oxidation of Fe_3O_4 to the more resistive γ-Fe_2O_3.

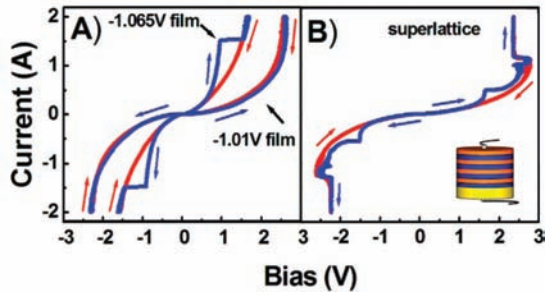

Figure 3. Resistance switching of magnetite films (A) and a magnetite superlattice (B) on Au(111) at 77 K. The *iV* curves were run with the current flowing perpendicular to the films by scanning the applied current at 50 mA/s. In each curve, the forward scan is blue and the reverse scan is red. The magnetite films in (A) were grown at −1.01 and −1.065 V to a thickness of 5 μm. The magnetite superlattice in (B) was produced by pulsing between −1.01 V for 1.5 s and −1.065 V for 0.5 s with a modulation wavelength of 12.2 nm, 354 bilayers, and a total thickness of 4.3 μm. Only the superlattice shows the negative differential resistance (NDR) feature due to the field-assisted insulator-to-metal phase transition.

The *iV* curve for the superlattice with a modulation wavelength of 12.2 nm shown in Figure 3B is richer in features than that of the individual films due to the nanolayering of the superlattice. It shows two low-to-high resistance switches at applied biases of +1.7/−1.5 V and +2.4/−2.3 V. We assume that these first two transitions are associated with the electrochemical oxidation of Fe_3O_4 to the more resistive γ-Fe_2O_3 at the contact/film interface as proposed by Odagawa et al.[8a] Following the second of these low-to-high resistance switches, the curve shows oscillations of the bias voltage, followed by a negative differential resistance (NDR) feature at +2.7/−2.6 V. The resistance of the superlattice abruptly decreases after the NDR feature, as shown by the near-vertical increase in current to the 2A limit of our instrument following the NDR feature. This final high-to-low resistance switch is consistent with the insulator-to-metal phase transition of the Verwey transition. The NDR feature is only present in superlattices with small modulation wavelengths. When the modulation wavelength is increased to 50 nm, the NDR feature disappears (see Figure S6).

Because both the applied electric fields ($\sim 10^6$ V/m) and the resulting currents (~1 A) are large in the resistance switching experiments, it is difficult to determine whether the insulator-to-metal transition in the superlattices is caused by Joule heating of the sample (from 77 K to greater than the Verwey transition temperature) or to an electric-field-driven transition that is due to strong electron−phonon coupling. Our measurements do show, however, that the transition is not due entirely to Joule heating, because the magnetite films deposited at −1.01 and −1.065 V vs Ag/AgCl do not undergo the insulator-to-metal transition, even though the power dissipated by the samples is as large as that of the superlattice. For the magnetite film deposited at −1.01 V vs Ag/AgCl, the Verwey transition temperature is 103 K, compared with 121 K for the superlattice, so it should take less power dissipation to raise the sample above the Verwey transition, yet the insulator-to-metal transition is not observed.

The insulator-to-metal phase transition in the superlattice may be facilitated by residual strain in the superlattice. Because of the lattice mismatch between the two layers in the superlattice, the alternating layers have 0.37% compressive and 0.37% tensile strain. These alternating strain fields will lower the symmetry of the system so that the structure of the magnetite more closely resembles the monoclinic low-temperature phase below the Verwey transition than the high-temperature cubic phase, resulting in a more kinetically labile phase transition. The alternating strain fields may also affect electron−phonon interaction. Below the Verwey transition, magnetite is in a charge ordered state with strong coupling of phonons to conduction electrons.[9] As suggested by other researchers,[2,10] the applied electric field may break down the charge-ordered state in the material. In our experiments this transition occurs with the nanolayered superlattice, but not with the individual films. The fact that multiple resistance states can be accessed by simply varying the applied bias opens up new possibilities for multibit data storage and retrieval.

Acknowledgment. This work was supported by the U.S. Department of Energy, Office of Basic Energy Sciences under Grant No. DE-FG02-08ER46518.

Supporting Information Available: Methods and materials, linear sweep voltammograms, Verwey transition temperatures, and additional resistance switching results. This material is available free of charge via the Internet at http://pubs.acs.org.

References

(1) (a) Waser, R.; Aono, M. *Nat. Mater.* **2007**, *6*, 833–840. (b) Sawa, A. *Mater. Today* **2008**, *11*, 28–36. (c) Szot, K.; Speier, W.; Bihlmayer, G.; Waser, R. *Nat. Mater.* **2006**, *5*, 312–320. (d) Yang, Y. C.; Pan, F.; Liu, Q.; Liu, M.; Zeng, F. *Nano Lett.* **2009**, *9*, 1636–1643.
(2) (a) Lee, S.; Fursina, A.; Mayo, J. T.; Yavuz, C. T.; Colvin, V. L.; Sofin, R. G. S.; Shvets, I. V.; Natelson, D. *Nat. Mater.* **2008**, *7*, 130–133. (b) Fursina, A. A.; Sofin, R. G. S.; Shvets, I. V.; Natelson, D. *Phys. Rev. B* **2009**, *79*, 245131/1–245131/6.
(3) Verwey, E. J. W. *Nature* **1939**, *144*, 327–328.
(4) (a) Switzer, J. A.; Hung, C.-J.; Breyfogle, B. E.; Shumsky, M. G.; Van Leeuwen, R.; Golden, T. D. *Science* **1994**, *264*, 1573–1576. (b) Switzer, J. A.; Shane, M. J.; Phillips, R. J. *Science* **1990**, *247*, 444–446. (c) Kothari, H. M.; Vertegel, A. A.; Bohannan, E. W.; Switzer, J. A. *Chem. Mater.* **2002**, *14*, 2750–2756.
(5) (a) Kulp, E. A.; Kothari, H. M.; Limmer, S. J.; Yang, J.; Gudavarthy, R. V.; Bohannan, E. W.; Switzer, J. A. *Chem. Mater.* **2009**, *21*, 5022–5031. (b) Kothari, H. M.; Kulp, E. A.; Limmer, S. J.; Poizot, P.; Bohannan, E. W.; Switzer, J. A. *J. Mater. Res.* **2006**, *21*, 293–301.
(6) Bard, A. J.; Faulkner, L. R. *Electrochemical Methods: Fundamentals and Applications*; Wiley: New York, 2001; p 340.
(7) (a) Burch, T. J.; Craig, P. P.; Hedrick, C.; Kitchens, T. A.; Budnick, J. I.; Cannon, J. A.; Lipsicas, M.; Mattis, D. *Phys. Rev. Lett.* **1969**, *23*, 1444–1447. (b) Freud, P. J.; Hed, A. Z. *Phys. Rev. Lett.* **1969**, *23*, 1440–1443.
(8) (a) Odagawa, A.; Katoh, Y.; Kanzawa, Y.; Wei, Z.; Mikawa, T.; Muraoka, S.; Takagi, T. *Appl. Phys. Lett.* **2007**, *91*, 133503/1–133503/3. (b) Kim, T. H.; Jang, E. Y.; Lee, N. J.; Choi, D. J.; Lee, K.-J.; Jang, J.-T.; Choi, J.-S.; Moon, S. H.; Cheon, J. *Nano Lett.* **2009**, *9*, 2229–2233.
(9) (a) Piekarz, P.; Parlinski, K.; Oles, A. M. *Phys. Rev. Lett.* **2006**, *97*, 156402/1–156402/4. (b) Huang, D. J.; Lin, H.-J.; Okamoto, J.; Chao, K. S.; Jeng, H.-T.; Guo, G. Y.; Hsu, C.-H.; Huang, C.-M.; Ling, D. C.; Wu, W. B.; Yang, C. S.; Chen, C. T. *Phys. Rev. Lett.* **2006**, *96*, 096401/1–096401/4.
(10) Sugimoto, N.; Onoda, S.; Nagaosa, N. *Phys. Rev. B* **2008**, *78*, 155104/1–155104/5.

JA909295Y